A method to evaluate the capillary stress tensor at failure in unsaturated soils

Florent Prunier, Denis Branque, Jérôme Duriez, Félix Darve

ARTICLE TEMPLATE

A method to evaluate the capillary stress tensor at failure in unsaturated soils

Florent Prunier[a], Denis Branque[b], Jérôme Duriez[c], Félix Darve[d]

[a]Université de Lyon, INSA Lyon, Laboratoire GEOMAS
[b]Université de Lyon, ENTPE, LTDS
[c]INRAE, Aix Marseille Univ, RECOVER, Aix-en-Provence, France
[d]Lab. 3S-r, UGA, Grenoble INP

ARTICLE HISTORY
Compiled December 19, 2023

ABSTRACT
This paper aims to provide a better understanding of the mechanisms that make it difficult to interpret the behavior of unsaturated soils using an effective stress principle. The main difficulty is that some deformed states of the unsaturated medium may not be statically admissible in saturated conditions. Therefore, we introduce the notions of total strain, which is measured at the boundary of the sample; effective strain, which is conjugated to the effective stress of the solid skeleton; and capillary strain, which results from the capillary forces. Recent results using the discrete element method prove that the effective strain can still be identified with the total strain in "small" strains and at failure. Consequently, we propose to interpret the behavior of unsaturated soils on the basis of the principle of effective stress revisited with the theory of multiphase media and to identify the total and effective strain tensors in a first simplified approach. A conceptual experimental procedure is proposed to assess what we call the capillary tensor, using existing experimental devices. We propose certain hypotheses that allow engineers to numerically bound this capillary tensor at failure by knowing the total stress state measured at failure and the effective failure envelope in saturated conditions.

KEYWORDS
Unsaturated soils, effective stress concept, capillary tensor, triaxial test

1. Introduction

To our knowledge, two main approaches have been developed to describe the behavior of unsaturated media in recent decades:

- the extended effective stress principle of Bishop and Blight (1963). It is well established that to consider only the scalar suction and the air pressure does not allow a good description of the actions of the fluid phases on the solid skeleton even by introducing an ad-hoc χ function as in (e.g. Arairo, Prunier, Djéran-Maigre, & Darve, 2012; Khalili & Khabbaz, 1998; Nikooee, Habibagahi, Hassanizadeh, & Ghahramani, 2013) or by introducing the notion of effective saturation degree (e.g. E. Alonso, Pereira, Vaunat, & Olivella, 2010; Schwan, 2023). The term

CONTACT F. Prunier. Email: florent.prunier@insa-lyon.fr

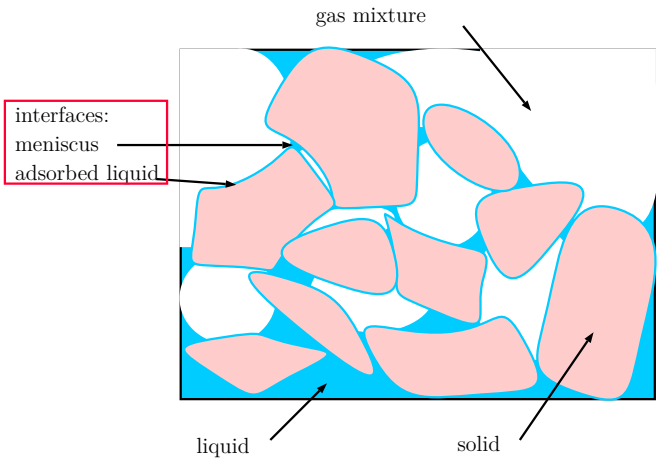

Figure 1. Conceptual diagram of an unsaturated granular medium
Alt Text: Diagram of a porous media highlighting grains and pores filled by air and liquid bridges.

"solid skeleton" is used here to refer to the solid material containing its voids and excluding any fluid-solid interface as introduced by Coussy (2004).

- the Barcelona Basic Model (E.E. Alonso, Gens, & Josa, 1990) and its most recent extensions, such as (e.g. Bruno, Gallipoli, & Mendes, 2021; Rojas & Chávez, 2013; Weber, Romero, & Lloret, 2022), which describe the unsaturated soil behavior using generalized stress variables in the form of a net stress $\boldsymbol{\sigma^{net}} = \boldsymbol{\sigma} - u_a \boldsymbol{I}$ and an effective stress $\boldsymbol{\sigma}$". $\boldsymbol{\sigma}$ is the total stress tensor, u_a the air pressure, and $\boldsymbol{I}$ the identity tensor. We note here the effective stress $\boldsymbol{\sigma}$", since the latter is supposed to act on the skeleton, which includes the solid skeleton plus the fluid-solid interfaces in the form of adsorbed water and menisci (e.g. Coussy, 2004; Coussy & Dangla, 2002). See figure 1 for a qualitative description of an unsaturated granular medium and the fluid-solid interfaces.

In fact, it was natural to want to describe the behavior of unsaturated soils with measurable quantities, in the same way as Terzaghi (1936) advocated in his principle of effective stress for saturated soils:

All the measurable effects of a change of stress, such as compression, distortion, and a change of shearing resistance are exclusively due to changes in the effective stresses σ'_1, σ'_2, *and* σ'_3.

However, we find that these two approaches are not really used in practice. There are several reasons for this:

- the ratio between the cost of characterizing unsaturated soil behavior and the gain from designing a geotechnical structure that takes into account the beneficial effects of unsaturated states is generally unsatisfactory.
- experimental devices for measuring or controlling suction are difficult to implement and insufficient. Furthermore, in terms of the Barcelona approach, the constitutive law for the skeleton (namely the solid skeleton plus its fluid-solid interfaces) turns out to be extremely complex.

Therefore, we propose to analyze the mechanical behavior of unsaturated soils in the framework of the multiphase media theory as developed by Madeo, dell'Isola, and Darve

(2013). Nevertheless, we restrict our work to granular soils and silts, excluding swelling clays such as smectites. It is likely that this approach can be extended to clays that are not water sensitive, such as kaolinites. As demonstrated in section 2, Terzaghi's effective stress principle for saturated soils fits perfectly into the framework of this theory. For unsaturated soils, we observe that this theory allows an extension of an effective stress principle, but by introducing a nonlinear decomposition of the strain tensor in the following form:

$$\boldsymbol{\varepsilon} = F\left(\boldsymbol{\varepsilon'}, \boldsymbol{\varepsilon^{cap}}\right) \tag{1}$$

In our opinion, this decomposition is one of the original features of this work, and is presented in detail in section 2.3. In the rest of the paper, bold letters designate tensors whose order will be specified in the text. Here, $\boldsymbol{\varepsilon}$ is the 2^{nd} order strain tensor measured at the boundary of a homogeneous soils sample, $\boldsymbol{\varepsilon'}$ is the strain tensor conjugated to the effective stress tensor by the strain energy of the solid skeleton, and $\boldsymbol{\varepsilon^{cap}}$ is the strain tensor resulting from the deformation action of all the various liquid-gas and solid-fluid finite interfaces. Nevertheless, this paper demonstrates that the exploitation of this theory of multiphase media in an experimental context is currently complicated. To our knowledge, there are no experimental devices that allow direct measures of the physical quantities involving the constitutive law of each phase: that of the solid skeleton, that of the liquid phase, and that of the gas phase. This paper does not present any innovation on experimental devices that would allow a better understanding of the behavior of unsaturated soils. Nevertheless, in section 2 we make a qualitative presentation of the latest theoretical developments that should, in our opinion, enable a simpler understanding and description of unsaturated soil behavior. We hope that the theoretical developments proposed in section 2 will assist in better understanding this complex behavior and could help in future research to:

- provide new ideas in interpreting data from standard experimental set-ups
- take these new conceptual developments into account when designing future advanced experimental set-ups, such as those that will soon enable us to finely characterize the evolution of the microstructure of the solid and fluid phases during laboratory tests.

Therefore, notwithstanding the experimental difficulties specified in the theoretical part, we propose in section 3 a conceptual experimental procedure that should make it possible to quantitatively assess the capillary effects on the solid skeleton with existing experimental devices. This procedure relies on the strong assumption of a pure identification of the total strain tensor with the effective strain tensor. After having presented a work mainly in conceptual form, in section 4 we propose certain assumptions that allow engineers to quantitatively evaluate the components of the capillary tensor at failure. These assumptions allow the strength of the unsaturated soil to be quantified even at low saturation, where an assumption of a spherical capillary tensor may no longer be relevant. Finally, section 5 presents an experimental campaign carried out on an unsaturated silt using a simple device. Results at failure are analyzed using the assumptions previously formulated in section 4.

2. Some remarks about the effective stress concept

The mechanical behavior of "monophasic" (i.e., saturated drained) granular materials is currently well understood and simulated by phenomenological elasto-visco-plastic constitutive relations (e.g. Christoffersen & Hutchinson, 1979; Colman & Gurtin, 1967; Desai & Siriwardane, 1984; DiMaggio & Sandler, 1971), homogenization techniques (e.g. Eshelby, 1957; Mori & Tanaka, 1973; Oller, 2014), and discrete element method (DEM) modelling (e.g. Froiio & Roux, 2011; Roux & Combe, 2002; Sibille, Hadda, Nicot, Tordesillas, & Darve, 2015).

For biphasic granular media, the relevance of Terzaghi's principle has been clearly established in geomechanics through experimental and theoretical approaches. The total stress $\boldsymbol{\sigma}$ can be additively decomposed into a so-called effective stress (i.e. the solid skeleton stress) $\boldsymbol{\sigma'}$ and an interstitial spherical fluid pressure $u\boldsymbol{I}$, with $\boldsymbol{I}$ the identity tensor:

$$\boldsymbol{\sigma} = \boldsymbol{\sigma'} + u\boldsymbol{I} \tag{2}$$

The effective stress appears to be the proper stress variable to express the constitutive behavior of the solid skeleton with its energy-conjugated total strain. The energy conjugate effective strain is equal here to the total strain, since it is clear that there is neither any capillary stress nor capillary strain in a saturated granular material without any liquid-gas interfaces. This has been very well verified by experiments (e.g. Skempton, 1954; Skempton & Bjerrum, 1957), and analytical homogenization techniques (e.g. Biot, 1955; De Buhan & Dormieux, 1996; Lade & De Boer, 1997). However, it is demonstrated later that in a general framework, neither the total stress nor the total strain (the one measured at the boundary of the soil) are constitutive variables; they are independent of each other and are not linked by any constitutive relationship. Moreover, undrained triaxial tests are usually simulated in the finite element method with a single-phase formulation by imposing the strain path. The response of the dry solid skeleton in terms of effective stresses is identical to the response of the solid skeleton subjected to the undrained hydro-mechanical path.

Let us consider a body constituted by three phases: a granular porous solid (subscript s), an interstitial isotropic liquid (subscript w), and an interstitial isotropic gas (subscript a). The figure 1 provides a conceptual diagram of an unsaturated granular medium.

In line with the surface tension phenomena, certain finite separation areas exist between these three immiscible phases, as follows: S_{sa} between solid and gas, S_{sw} between solid and liquid, and S_{aw} between gas and liquid. Therefore, it is not possible to apply the mixture theory, which basically assumes an intimate mixture between both fluids. Bishop's equation, in which the parameter χ is taken as the saturation degree S_r, is therefore not valid here:

$$\boldsymbol{\sigma'} = \boldsymbol{\sigma} - u_a\boldsymbol{I} + S_r\left(u_a - u_w\right)\boldsymbol{I} \tag{3}$$

where u_a and u_w are the gas and liquid pressures, respectively. Furthermore, the more general Bishop relationship, where χ is an ad hoc coefficient to be measured in experi-

ments, seems impossible to define objectively in practice.

$$\boldsymbol{\sigma}' = \boldsymbol{\sigma} - u_a \boldsymbol{I} + \chi \left(u_a - u_w \right) \boldsymbol{I} \tag{4}$$

Indeed, the existence of finite separation surfaces between liquid and gas implies two consequences:

(1) The fluids stress tensor is not spherical, being impossible to describe with equation (4). The fluids stress must be considered as a true capillary stress tensor, which possesses deviatoric components (i.e., it is a non-spherical matrix). This is quite obvious from a micro-mechanical point of view if we consider the distribution of menisci inside the body. In fact, it is well known that the distribution of granular contacts is not isotropic as soon as a deviatoric loading is applied to a granular assembly due to the induced anisotropy, which is particularly strong for granular materials. In the same way, the distribution of menisci will not be isotropic in a three-phasic medium. Therefore, the capillary stress induced by these menisci will not be isotropic, thus contradicting Bishop's relationship 4.

(2) For specific configurations, where the fluid stress tensor is spherical, Bishop's relationship reduces the interface effects to a function χ times the suction $s = u_a - u_w$, while micro-mechanical approaches (e.g. Chateau & Dormieux, 1995; Duriez, Eghbalian, Wan, & Darve, 2017; Farahnak et al., 2021; Zhou et al., 2019) prove that an additional term that depends on the air-water surface tension γ_{aw} cannot be neglected. This last point is developed in the next section.

2.1. Insight into the stress concept for unsaturated soils with a multiphasic theory

If the mixture theory cannot be applied for partially saturated granular media, it is necessary to come back to the general theory of multiphasic media, as done by Madeo et al. (2013).
The first step is to define the deformations of each phase and their energy conjugate stresses:

- $\boldsymbol{\varepsilon_s}$ and $\boldsymbol{\sigma_s}$ for the anisotropic solid skeleton,
- ε_w and u_w for the isotropic liquid,
- ε_a and u_a for the isotropic gas.

The constitutive behavior and the associated potential energy of each phase can then be defined in this second step. For the purposes of simplicity, we can assume here that the porous solid is hyper-elastic. Cowin and Nunziato (1983) elastic relation is a possible solution with five constitutive parameters (thus three additional parameters with respect to Hooke's linear isotropic relation to take into account the variable porosity). Let us note that the elastic law of the porous solid skeleton must definitely be distinguished from the elastic law of the homogeneous non-porous solid matter. The state equations for the liquid and the gas are classical and well established with, for example, function of their respective quadratic potentials.

A third step takes into account the conservation laws for the phase masses and the momentum balance equations for the phases. The total energy of the system is assumed to be equal to the sum of the phase potential energies, the interface potential energies, and the phase kinetic energies minus the externally imposed work. The final

equation comes from the application of the least action principle in the framework of variational methods.

This set of equations is, however, not closed, and it is necessary to describe the inter-phase interactions, such as, for example, Laplace's equation:

$$s = u_a - u_w = \gamma_{aw}\ div\,(\vec{n}) \tag{5}$$

where $\vec{n}$ is the outward normal of the air-water interface and s the suction. In the case of a spherical surface (air bubble) of radius R, we would obtain:

$$s = u_a - u_w = 2\gamma_{aw}/R \tag{6}$$

Equation (5) or equation (6) is one of the discontinuity equations at the various phase separation surfaces that have to be taken into account to obtain a fully closed description of the system.

In order to gain a less abstract understanding of the conjugate quantities that enable a pertinent description of the behavior of the solid skeleton in the unsaturated domain, it is necessary to return to the granular nature of the medium under consideration.

2.2. Insight into the stress concept for unsaturated soils with the micro-mechanical "μ-unsat" approach

Denoting V_α the volume of the three bulk phases $\alpha = a, s, w$ and $\alpha\beta$ any interface extending over the surface $S_{\alpha\beta}$ with $\alpha, \beta \in \{a, w, s\}$, internal forces exist in all those volumes V_α and interfaces $S_{\alpha\beta}$ (through surface tension phenomena) and combine to form the total stress $\boldsymbol{\sigma}$ that corresponds to the loads exerted onto the boundaries of an unsaturated representative elementary volume (REV):

$$\boldsymbol{\sigma} = \frac{1}{V}\left[\sum_{\alpha=a,s,w}\int_{V_\alpha}\boldsymbol{\sigma_\alpha}\ dV + \sum_{\alpha,\beta=a,s,w}\int_{S_{\alpha\beta}}\boldsymbol{\pi_{\alpha\beta}}\ dS\right] \tag{7}$$

As demonstrated by Chateau and Dormieux (1995); Gray and Schrefler (2007); Gurtin and Murdoch (1975), appropriate interface stress tensors $\boldsymbol{\pi_{\alpha\beta}}$ should express according to the surface tension coefficient $\gamma_{\alpha\beta}$ and a projection tensor $(\boldsymbol{I} - \vec{n} \otimes \vec{n})$ with $\vec{n}$ the normal to $S_{\alpha\beta}$: $\boldsymbol{\pi_{\alpha\beta}} = \gamma_{\alpha\beta}(\vec{n} \otimes \vec{n} - \boldsymbol{I})$. The stresses within the fluid phases $\alpha = a, w$ are $\boldsymbol{\sigma_\alpha} = u_\alpha \boldsymbol{I}$, while the stress $\boldsymbol{\sigma_s}$ inside the solid phase can be classically obtained from the tractions acting onto the individual soil grains of total surface S_s since (assuming mechanical equilibrium under no gravity):

$$\int_{V_s}\boldsymbol{\sigma_s}\ dV = \int_{S_s}(\boldsymbol{\sigma_s}\,\vec{n}) \otimes \vec{x}\ dS = \int_{S_s} -\vec{t} \otimes \vec{x}\ dS \tag{8}$$

After considering all relevant tractions $\vec{t}$ in Eq. (8), that is, solid-solid contact forces, fluid pressure loads, as well as surface tension forces onto the solid grains, and algebraic derivations assuming rigid solid grains and zero contact surfaces between them, the contribution of solid-fluid interfaces vanishes and the total stress can finally be expressed

as (Duriez et al., 2017; Duriez & Wan, 2016):

$$\boldsymbol{\sigma} - u_a\,\boldsymbol{I} = \boldsymbol{\sigma^{cont}} + \boldsymbol{\sigma^{cap}} = \frac{1}{V}\sum_c \vec{f}^c \otimes \vec{l} - \frac{1}{V}\left[s\left(V_w\,\boldsymbol{I} + \int_{S_{sw}} \vec{n}\otimes\vec{x}\;dS \right) + \gamma_{aw}\left(\int_{S_{aw}} (\boldsymbol{I} - \vec{n}\otimes\vec{n})\;dS + \int_\Gamma \vec{\nu}_{aw}\otimes\vec{x}\;dl \right) \right] \tag{9}$$

with:

$$\boldsymbol{\sigma^{cont}} = \frac{1}{V}\sum_c \vec{f}^c \otimes \vec{l} \tag{10}$$

$$\boldsymbol{\sigma^{cap}} = - \frac{1}{V}\left[s\left(V_w\,\boldsymbol{I} + \int_{S_{sw}} \vec{n}\otimes\vec{x}\;dS \right) + \gamma_{aw}\left(\int_{S_{aw}} (\boldsymbol{I} - \vec{n}\otimes\vec{n})\;dS + \int_\Gamma \vec{\nu}\otimes\vec{x}\;dl \right) \right] \tag{11}$$

In the rest of this paper, we assume a constant uniform air pressure u_a, serving as reference. This assumption covers most geotechnical applications, and we obtain the following simple expression of $\boldsymbol{\sigma}$.

$$\boldsymbol{\sigma} = \boldsymbol{\sigma^{cont}} + \boldsymbol{\sigma^{cap}} \tag{12}$$

This additive relation has been very carefully verified by DEM computations of Duriez and Wan (2017b) in the case of a pendular regime.

Eqs (9) to (11) first involves the contact stress $\boldsymbol{\sigma^{cont}}$, function in Eq. (10) of the contact force $\vec{f}^c$ as sustained by 2 from 1 in a 1-2 contact c and of the branch vector $\vec{l}$ pointing from the center of mass of 1 to the center of mass of 2. This stress tensor equals the total stress in dry conditions, as well as the classical effective stress in saturated conditions. Its constitutive role in unsaturated conditions is discussed later on. The remainder of the total stresses are encompassed in a capillary stress $\boldsymbol{\sigma^{cap}}$ with various tensorial terms. These tensorial terms describe the internal forces within the fluids and interface phases, as well as the mechanical interactions between the solid phase and the other phases. In Eq. (11), for example, one should note the oriented action of suction s along wetted surfaces S_{sw} with $\vec{n}$ the outward solid normal and $\vec{x}$ being possibly expressed from each particle centroid; together with an oriented action of surface tension within the contractile skin S_{aw} and along contact lines Γ where the three phases meet, with $\vec{\nu}$ being the inwards conormal to S_{aw}. We emphasize that this last term (factor of γ_{aw}) is not taken into account in Bishop's expression.

2.3. Concluding remarks about the constitutive stress and strain variables in unsaturated soils

$\boldsymbol{\sigma^{cont}}$ corresponds to the solid skeleton stress. It could be called effective stress and denoted as $\boldsymbol{\sigma'}$ in the sense that this stress has to be used to express the solid skeleton

constitutive relation. We simplify the notations of equation (12) as follows :

$$\boxed{\boldsymbol{\sigma} = \boldsymbol{\sigma'} + \boldsymbol{\sigma^{cap}}} \tag{13}$$

Moreover, it should be noted that this stress also corresponds to what is commonly called "effective stress" in saturated conditions.

$\boldsymbol{\sigma^{cap}}$ has until now been called the capillary stress. It results from the isotropic state equations of the liquid and the gas, and the structural strength of the liquid/gas interfaces. Consequently, there is no energy conjugate capillary strain for this structural system, which is multiphasic. Therefore, no constitutive equation linking capillary stress and capillary strain can be considered. As regards the strains of the system, we can only expect to have a relationship between total strain, effective strain, air volume variation, water volume variation and liquid-gas interface variations. A second observation concerns the fact that the capillary stress is decomposed additively into two stresses according to equation (11): the first is proportional to the suction $s = u_a - u_w$ and the second is proportional to the surface tension coefficient. This is precisely what we observe from the point of view of physics. Indeed, the attractive capillary force has two origins: (i) the pressure difference between liquid and gas, giving rise to the first term; and (ii) the surface tension stress on the liquid-gas interface, inducing the second term.

A final observation relates to the non-additive decomposition of the total strain in an effective part and a capillary part. A sketch of such a non-additive decomposition of the total strain is presented in figure 2. The non-additive decomposition of the total strain tensor is probably one of the main difficulties to overcome from a practical point of view. In fact, the "effective strain" is almost inaccessible from a practical point of view (i.e., in the absence of an advanced $3D$ scanning imagery device). Only the "total strain" is easily accessible experimentally. A second important difficulty is that the set of statically admissible geometrical configurations in the saturated case is strictly included inside the set of statically admissible geometrical configurations in an unsaturated case. Figure 2 also highlights this problem. In other words, a constitutive model identified and verified in saturated configurations does not encompass all the admissible geometrical configurations of certain unsaturated cases. Consequently, the existence of a constitutive law of the solid skeleton under unsaturated conditions becomes a tangible question that we do not open in this work. This is what makes it so difficult to build a general constitutive model that is also suitable for unsaturated conditions. Nevertheless, assuming a full identification of the "total strain" with the "effective strain", verifications and discussions of the use of the contact stress as an effective stress have been proposed along different loading paths in Duriez and Wan (2018); Duriez, Wan, Pouragha, and Darve (2018) in the pendular regime with spherical particles. In fact, this assumption seems quite reasonable, at least for dense soils where few of the contact losses that occur in the unsaturated case can be expected to be inaccessible in the saturated case.

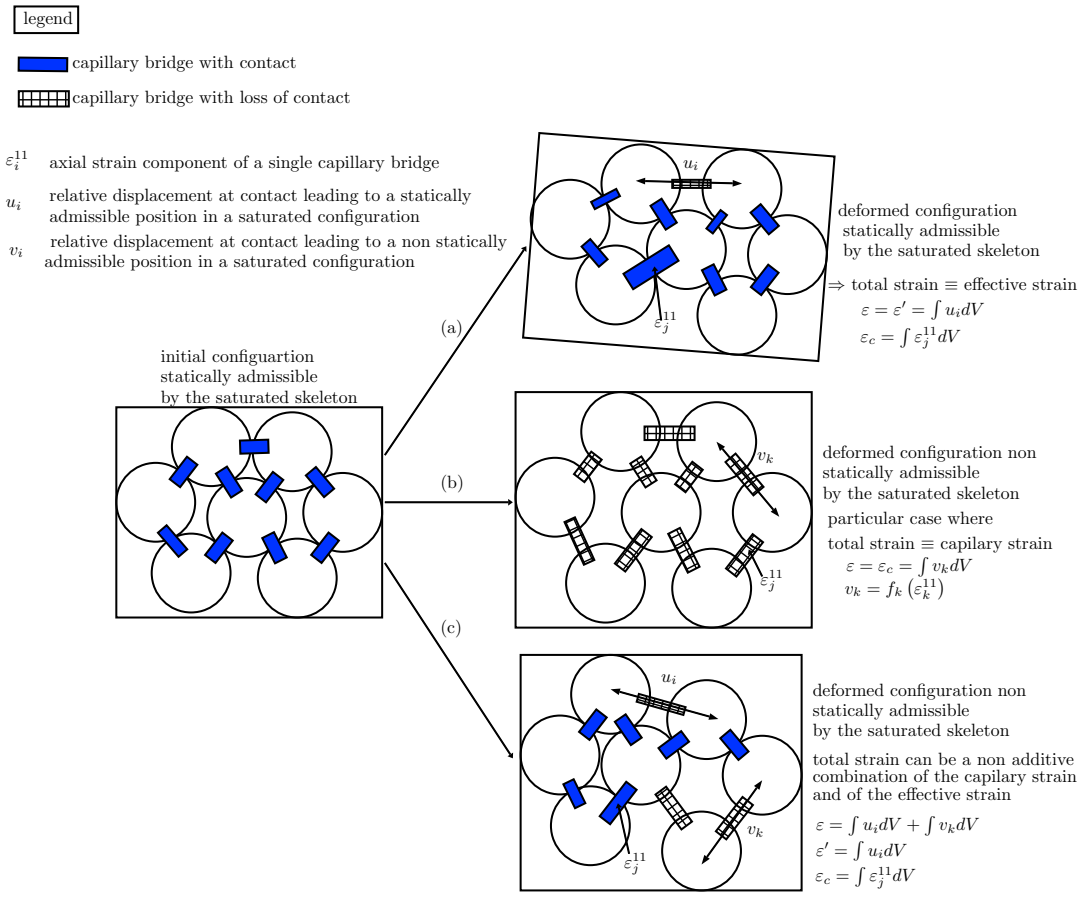

Figure 2. Diagram of strain decomposition in an unsaturated soil showing three possible strain regimes with different proportions of effective (ε') and capillary (ε_c) strains in the total strain (ε). Grains and capillary bridges are represented schematically by circles and rectangles. The sign $\int$ schematically denotes a summation operation, but is not properly mathematically defined in this sketch.
Alt Text: 4 pictures of a sample of grains with liquid bridges.
Long description: On the left an initial configuration with liquid bridges at each contact. On the top right a deformed configuration statically admissible in a saturated state. On the middle right a deformed configuration non statically admissible in a saturated configuration: every contact is lost. The equilibrium is done only with liquid bridges in tension. On bottom right a deformed configuration non statically admissible in saturated condition with some contact losses.

2.4. Constitutive role of the effective stress when associated with the total strain

Discrete element method approaches enable a thorough investigation of these stress tensors in the case of an ideal unsaturated granular soil with spherical particles and in the pendular regime. They first evidenced a clear tensorial (i.e., spherical and deviatoric) nature of $\boldsymbol{\sigma'}$ as soon as the microstructure was not completely isotropic - during triaxial compressions, for example. See Duriez and Wan (2017a); Scholtes, Hicher, Nicot, Chareyre, and Darve (2009).

The effective stress $\boldsymbol{\sigma'}$ was also investigated for its constitutive stress-strain-strength role in unsaturated conditions. Duriez et al. (2018) demonstrated that the limit states of $\boldsymbol{\sigma'}$ did coincide in time with the limit states of the total stress $\boldsymbol{\sigma}$ along conventional drained triaxial loading paths $\sigma_2 = \sigma_3 = cst$ and that the corresponding failure line in terms of effective stress was unique in dry and unsaturated conditions, when examining two different packing densities. This unique failure description had also been previously proposed on the basis of DEM by Duriez et al. (2017); Duriez and Wan (2017a); Scholtes et al. (2009), as well as on the basis of experimental data by E. Alonso et al. (2010); Khalili and Khabbaz (1998); Lu and Likos (2006), thus making it possible to consider the effective stress as an appropriate stress-strength effective stress.

In terms of stress-strain behavior when assuming that $\boldsymbol{\varepsilon'} \equiv \boldsymbol{\varepsilon}$ (i.e., when defining strains from the boundaries of an unsaturated REV), Duriez and Wan (2018); Duriez et al. (2018) compared the resulting effective stress paths for given strain paths in dry or unsaturated conditions. The comparison indicated that the effective stress-total strain behavior was unique in limited cases, involving dense packings and contractant loading paths only. While this demonstrates that no complete constitutive stress-strain nature can be claimed for the effective stress associated with the total strain, a limited constitutive nature can still be considered for these specific cases. This makes it interesting in practice to estimate initial stiffnesses or possibly œdometric (over-consolidated) loading paths, as argued by E. Alonso et al. (2010).

In the rest of this paper, we assume that an effective stress can be associated with the total strain and propose a procedure for experimentally evaluating this capillary tensor with the use of standard devices.

3. A conceptual procedure to assess the capillary tensor

It must be stressed that the procedure described in this section is only conceptual, as we have not yet developed an œdometer or triaxial device to make such experiments possible. Assuming a complete identification of $\boldsymbol{\varepsilon'}$ and $\boldsymbol{\varepsilon}$, we can state that the effective stress governs the deformation of the solid skeleton by definition. Hence, if no technology exists to measure the capillary stress tensor $\boldsymbol{\sigma^{cap}}$, then the only way to assess $\boldsymbol{\sigma^{cap}}$ is to use its definition and to evaluate the difference $\boldsymbol{\sigma} - \boldsymbol{\sigma'}$ along a comparable effective strain path. An experimental procedure to assess the capillary tensor is proposed as follows: starting from a saturated state, a first desaturation path is followed until reaching a given initial degree of saturation; a loading path is then performed in unsaturated conditions. On a second identical soil sample, a second test under saturated conditions is then controlled by following exactly the same strain path from the initially saturated

conditions. The strain path is here understood to be controlled in every direction. In theory, the six components of the tensor should be imposed equal to the response of the first sample subjected to the unsaturated test. In practice, this will result in the three principal components for any homogeneous test in the orthotropy axes. In such a conceptual framework, the difference between $\boldsymbol{\sigma} - \boldsymbol{\sigma'}$ along the same strain path is relevant from a constitutive point of view. At the scale of the representative elementary volume (REV), expression (13) can be rewritten as follows:

$$\boxed{\boldsymbol{\sigma'} = \boldsymbol{\sigma} - \boldsymbol{\sigma^{cap}}\left(s, \gamma_{aw}, \boldsymbol{\lambda}\right)} \tag{14}$$

where $\boldsymbol{\lambda}$ is a vector of internal variables that would account for the granular microstructure, as well as for the fluid-solid interfaces microstructure and the liquid-gas interfaces microstructure. In a first simplified approach, $\boldsymbol{\lambda}$ can contain components or invariants of the plastic strain tensor $\boldsymbol{\varepsilon^p}$ only. From laboratory tests allowing a control or a measure of the suction, the difference between the total stress under unsaturated conditions and the effective stress under saturated condition provides the evolution of the capillary tensor $\boldsymbol{\sigma^{cap}}$ as a function of the state variables s and γ_{aw} and of internal variables $\boldsymbol{\lambda}$. Nevertheless, the conditions allowing us to identify the total strain with the effective strain as a constitutive tensor conjugated to the effective stress tensor have to be more precise in future studies. In particular, the question that emerges is whether this assumption can be relevant over the whole range of a loading path to failure for certain dense or overconsolidated soils. For loose or normally consolidated soils, the results of the literature review presented in the first sections up to 2.4 reveal that this procedure is valid only for a small range of deformations in a quasi-elastic regime. We emphasize that with the procedure described above, the ability of the experimental set-up to be fully strain controlled from the initial state to failure is a good indicator of the validity of the hypothesis of identifying the total strain with the effective strain.

In concluding this experimental procedure, we observe that it works perfectly for saturated soils. Indeed, in this last case, the fluid-solid interface forces are self-balancing. Consequently, it is only the fluid pressure that plays a role at the scale of the REV, and the effective strain is moreover identified with the total strain. Therefore, drained triaxial tests at constant volume make it possible to highlight the phenomenon of dry liquefaction. In a saturated consolidated undrained triaxial test (C.U+u), the response of the material in effective stresses is exactly the same as in a dry, consolidated and drained triaxial test with constant volume (Darve, Arulanandan, & Scott, 1993; Lanier & Bloch, 1989). This has been verified in the experiments, and the procedure is commonly used in finite elements or discrete elements to reproduce the undrained response of saturated soils without implementing a hydro-mechanical coupling.

4. Practical assessment of the capillary tensor at failure

Measurement or control of suction is not necessary to evaluate the capillary tensor $\boldsymbol{\sigma^{cap}}$ at failure, unless identification with the state variables (s, γ_{aw}) and the internal variables $\boldsymbol{\lambda}$ is desired. Using classical experimental devices, the main difficulty is to know which total and effective stress states are comparable from a constitutive point of view.

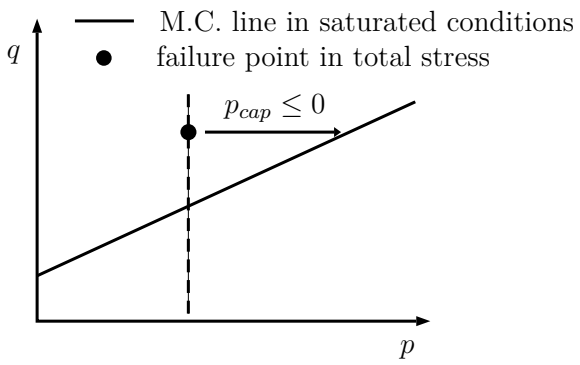

Figure 3. Sketch of the image point of effective failure stress states under the basic assumption: $\sigma_{ij}^{cap} = \sigma^{cap}\delta_{ij}$. The dashed line serves only to emphasize that p_{cap} is given by the offset along the p-axis between p_{tot} and p' when σ_{cap} is spheric.
Alt Text: $q-p$ plane with the effective Mohr-Coulomb line. One point in total stress outside of the effective admissible domain. From this point an horizontal arrow showing the projection permitting the computation of the capillary pressure.

If we assume a spherical capillary tensor for saturation degree in the vicinity of 1, we have:

$$\sigma_{ij}^{cap} = \sigma^{cap}\delta_{ij} \tag{15}$$

Hence, noting $q = \sigma_1 - \sigma_3$ with σ_1 the axial principal stress and σ_3 the radial principal stress, the classical result holds:

$$q = q' \tag{16}$$

When presenting the results in a $(q-p)$ plane, σ^{cap} is simply deduced by making the horizontal projection of the total stress state at failure on the Mohr-Coulomb line obtained in saturated conditions (see figure 3). In this last case, we have:

$$\boxed{\sigma^{cap} = p - p'} \tag{17}$$

The problem becomes more complicated when we want to consider a possible non-spherical capillary stress tensor. In that case, $q \neq q'$, we therefore propose a way to find a range for the values of the capillary tensor. A first basic assumption is to consider that

$$p^{cap} = \frac{1}{3}\left(\sigma_1^{cap} + 2\sigma_3^{cap}\right) \leq 0 \tag{18}$$

In fact, experimental evidence, as well as physical models developed for moistened granular media prove that $p^{cap} < 0$ in the capillary regime (near the saturation regime). For example, Rumpf (1962) proposed the following expression :

$$p^{cap} = -\frac{6}{\phi}\frac{S_r}{e}\frac{\gamma_{aw}}{d_p}\cos(\theta) \tag{19}$$

with ϕ a particle shape factor, d_p the apparent particle diameter and θ the the liquid

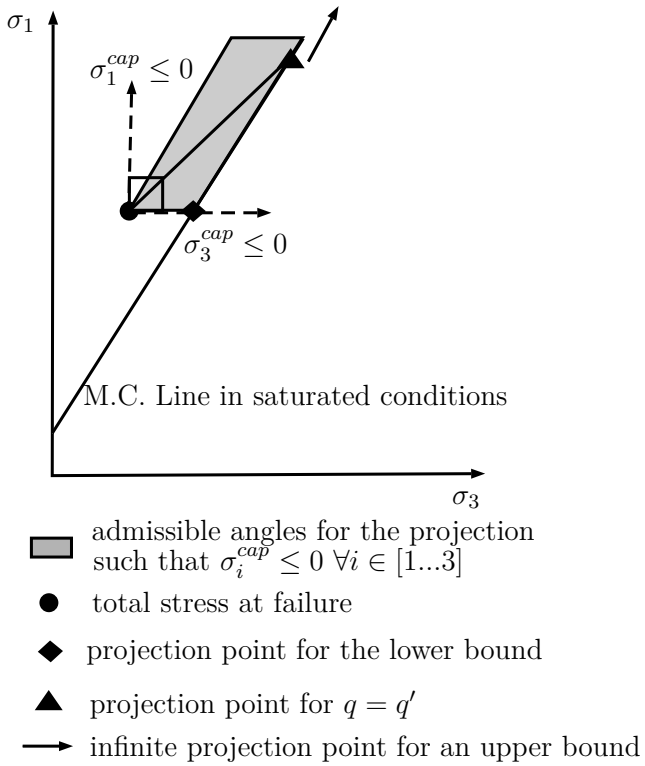

Figure 4. Sketch of possible image point of effective failure stress states under a basic assumption: $\sigma_i^{cap} \leq 0, \; \forall i \in \; [1,3]$.
Alt Text: $(\sigma_1 - \sigma_3)$ plane showing the possible projection on the effective More-Coulomb line to compute the components of the capillary tensor.

wetting angle. Consistent with DEM observations, we then assume that the total stress tensor and the capillary stress tensor are coaxial in the context of laboratory tests performed in the orthotropic axes, and we extend the first assumption to every eigenvalue of the capillary stress tensor:

$$\sigma_i^{cap} \leq 0, \; \forall i \in \; [1,3] \tag{20}$$

Indeed, in the case of the pendular regime (low saturation, no continuous liquid phase), each capillary bridge gives rise to an attractive resultant force between two grains. It therefore seems natural to consider that the sum of all these actions in a given direction provides a negative stress component. For the intermediate funicular regime, things seem less natural. Here, we assume a kind of continuity between each regime. We assume that a positive capillary stress component is possible only in saturated conditions. This set of hypotheses is summarized in figure 4. The value of $\boldsymbol{\sigma^{cap}}$ is denoted by $\boldsymbol{\sigma_{LB}^{cap}}$, which ensures a minimal value of q' on the effective Mohr-Coulomb failure line. In the same way the value of $\boldsymbol{\sigma^{cap}}$ is denoted by $\boldsymbol{\sigma_{UB}^{cap}}$, which ensures a maximal value of q' on the effective Mohr-Coulomb failure line.

4.1. A lower bound for $\boldsymbol{\sigma^{cap}}$

In the absence of any micro-mechanical results covering the full saturation range, a reasonable lower bound for the capillary stress tensor is obtained as follows:

$$q' \leq q \Leftrightarrow q^{cap} \geq 0 \tag{21}$$

$$\Leftrightarrow \sigma_1 - \sigma_1^{cap} - (\sigma_3 - \sigma_3^{cap}) \leq \sigma_1 - \sigma_3 \tag{22}$$

$$\Leftrightarrow \sigma_3^{cap} - \sigma_1^{cap} \leq 0 \tag{23}$$

as $\sigma_i^{cap} \leq 0 \; \forall \; i$ a maximum value of q^{cap} is reached for

$$\boxed{\sigma_{1LB}^{cap} = 0} \tag{24}$$

By using the Mohr-Coulomb relationship that holds for effective stress, we obtain the following:

$$\sigma_1' = \frac{1+\sin\varphi'}{1-\sin\varphi'}\sigma_3' + \frac{2C'\cos\varphi'}{1-\sin\varphi'} \tag{25}$$

$$\Leftrightarrow \sigma_1 = \frac{1+\sin\varphi'}{1-\sin\varphi'}(\sigma_3 - \sigma_{3LB}^{cap}) + \frac{2C'\cos\varphi'}{1-\sin\varphi'} \tag{26}$$

which provides:

$$\boxed{\sigma_{3LB}^{cap} = \sigma_3 + \frac{2C'\cos\varphi'}{1+\sin\varphi'} - \sigma_1\frac{1-\sin\varphi'}{1+\sin\varphi'}} \tag{27}$$

4.2. An upper bound for $\boldsymbol{\sigma^{cap}}$

An upper bound cannot be derived in the same way. With the help of figure 4, we can only conclude that when:

$$q' \geq q \Leftrightarrow q^{cap} \leq 0 \tag{28}$$

$$\Leftrightarrow \sigma_1 - \sigma_1^{cap} - (\sigma_3 - \sigma_3^{cap}) \geq \sigma_1 - \sigma_3 \tag{29}$$

$$\Leftrightarrow \sigma_3^{cap} - \sigma_1^{cap} \geq 0 \tag{30}$$

and we obtain an infinite minimum value of q^{cap} for:

$$\sigma_1^{cap} = -\infty \tag{31}$$

Therefore, micromechanical considerations about the particle size distribution, the maximum particle distance acceptable for a capillary bridge, and acceptable statistics

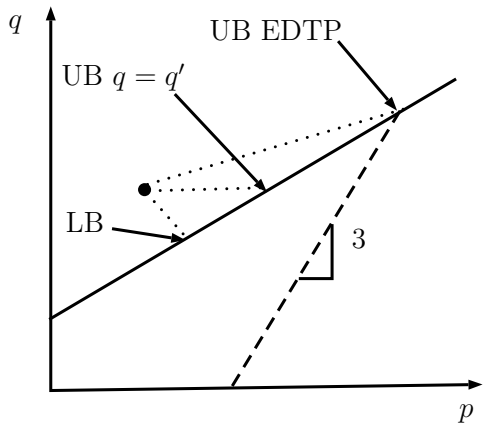

Figure 5. Range of effective stresses at failure to assess the capillary stress at failure. [LB]=lower bound, [UB q=q']=upper bound assuming a spherical capillary stress, [UB EDTP]=upper bound assuming an effective drained triaxial path.
Alt Text: $(q - p)$ plane showing the three assumed projections on the effective Mohr-Coulomb line to compute the components of the capillary tensor.

of the capillary bridge distribution seem to be necessary to derive such an upper bound. However, this is beyond the scope of the present work. Facing such difficulty, a conservative argument can be proposed in engineering practice. The spherical capillary tensor can be used as an upper bound of the capillary effects, since beyond this limit, $q' > q$ provides an increasing strength for the soil sample.

Finally, we present a last assumption to derive an upper bound for $\boldsymbol{\sigma}^{cap}$. In the study by Duriez et al. (2018), in which several DEM simulations of unsaturated drained triaxial tests under constant suction were performed, it was observed that the response in terms of the effective stress path is also a drained triaxial path. This observation needs to be confirmed by future research, but if we consider this to be true in all saturation regimes, then the next procedure can be used. First, an upper bound for the capillary pressure has to be assessed at the end of the isotropic phase. In engineering practice, we can assume that the initial value of the suction s_0 before any isotropic compression is an upper bound of the capillary pressure $p_0'^{cap}$ at the end of the isotropic compression. In fact, $\mathrm{Tr}\left(\boldsymbol{\sigma}^{\boldsymbol{cap}}\right)/3 = p^{cap} \leq s$ (e.g. Arairo et al., 2012), and we can assume in a first approach that s is not excessively affected by a drained isotropic compression. From this initial state, the effective failure state is obtained in a classical manner with the intersection of the Mohr-Coulomb envelope and the straight line of slope 3 in a (q, p) plane. In figure 5, we present the range of the possible image points that can be used on the effective Mohr-Coulomb envelope to assess the effective stress at failure, and therefore the capillary stress at failure. In concluding this section, we make the following observation. When performing three drained triaxial paths under a separate confining pressure with a controlled suction on an unsaturated soil, the failure points can sometimes be aligned in a $(q - p)$ plane or in the Mohr's plane. However, the apparent cohesion and the apparent friction angle expressed in total stress have no meaning from a constitutive point of view. Indeed, the components of the capillary tensor cannot be measured and are distinct in the three tests. This is exactly the same as measuring an undrained cohesion C_u when performing an unconsolidated and undrained test (U-U) on a saturated soil sample. C_u has no meanings from a constitutive point of view.

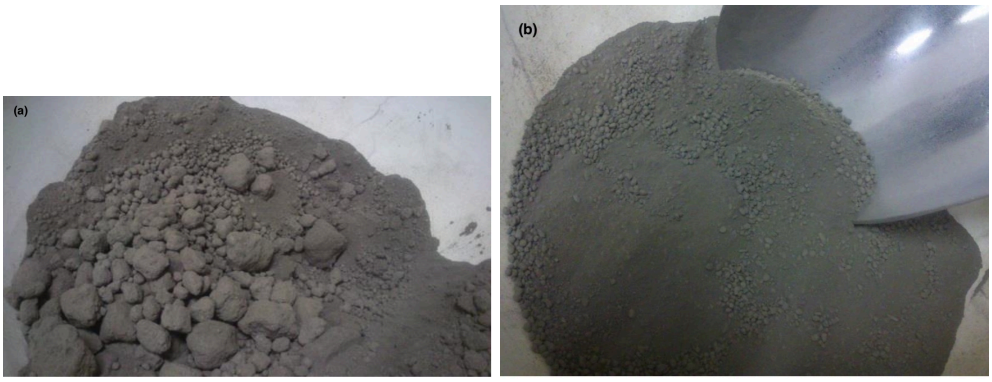

Figure 6. (a) Natural material of Gavet. (b) Passing fraction at 2 mm studied in this work. According to Hoang (2017).
Alt Text: 2 photographs of the Gavet silt. On the left the natural material. On the right the material with only particles smaller than 2 mm.

Finally, if we could impose the same capillary tensor for all three tests, the expressions for its components could be given in terms of apparent cohesion, effective cohesion, and effective friction angle, as presented in the Appendix 7. However, these formulas are useless in practice.

5. Experimental results analysis

In this section, we present the results of the drained triaxial tests that were performed on silt from Gavet, a village in the French Alps. A first campaign of characterization tests was carried out in the work of Hoang (2017). We then completed these tests with a series of unsaturated triaxial tests with measured initial suction.

5.1. Summary of the results from Hoang (2017)

A qualitative aspect of the studied material is presented in figure 6. The soil fraction finer than 20 mm is given in figure 7. In the present study, only particles smaller than 2 mm were taken into account in the experimental campaign (see figure 6 (b)). From the dry state in powder form, the samples were moistened and subjected to Proctor compaction tests under 25 shots. During these tests, suction was measured precisely with the filter paper method to determine the suction levels of the samples after compaction. This made it possible to plot the graph of the suction versus the mass water content ($w = M_w/M_s$), as presented in figure 8. A series of saturated drained triaxial tests was then performed. The samples were first compacted with the Proctor procedure under an average mass water content of $w = 10.5$ %, while the optimum Proctor was measured at $w = 12$ %. This permits to warrant an initial suction level about 55 kP_a and samples easy to shape. This led to an initial void ratio $e \approx 0.5$. The samples were then saturated inside the triaxial device.
A first series of isotropic compression was performed. The results are presented in the (e, p') curve (figure 9). This enables us to estimate the pre-consolidation pressure at approximately 200 kPa for the compaction protocol proposed above. Next, a series

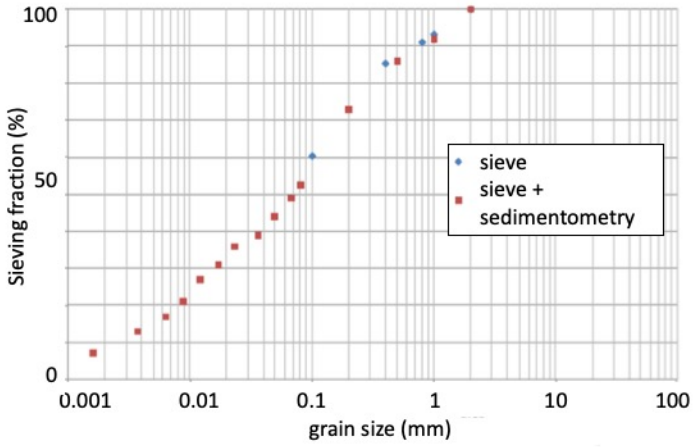

Figure 7. Particle size curve of the Gavet silt: fraction under 20 *mm*. According to Hoang (2017).
Alt Text: Particle size curve of the Gavet silt

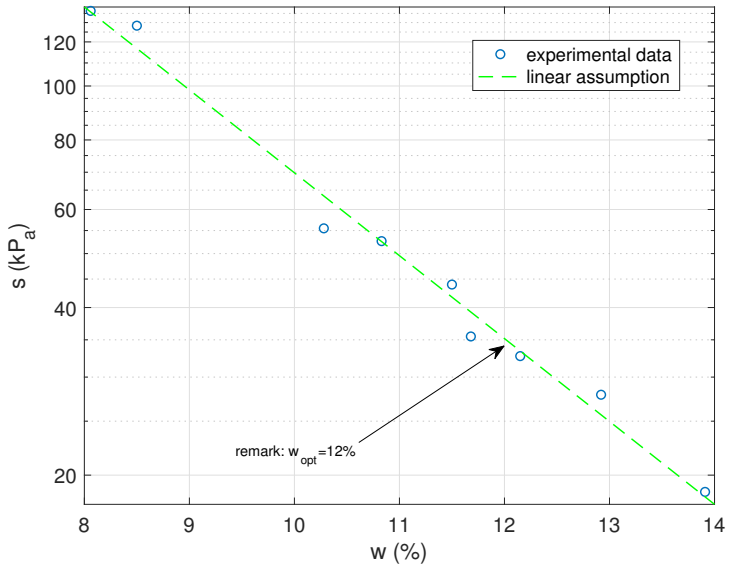

Figure 8. Evolution of the suction with the mass water content after Proctor tests. According to Hoang (2017).
Alt Text: Retention curve of the Gavet Silt showwing the evolution of the suction as a function of the mass water content.

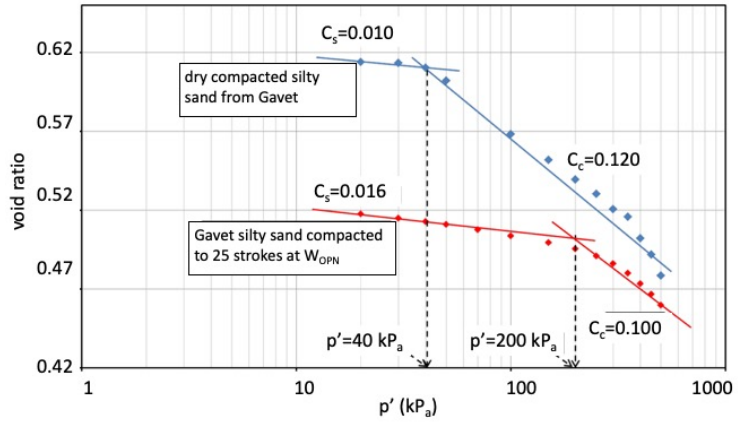

Figure 9. Evolution of the void ratio with the effective isotropic pressure - according to Hoang (2017). In the present paper, the compaction at the optimum Proctor is retained (red curve).
Alt Text: $(e - p')$ curve showing the isotropic response of the Gavet silt.

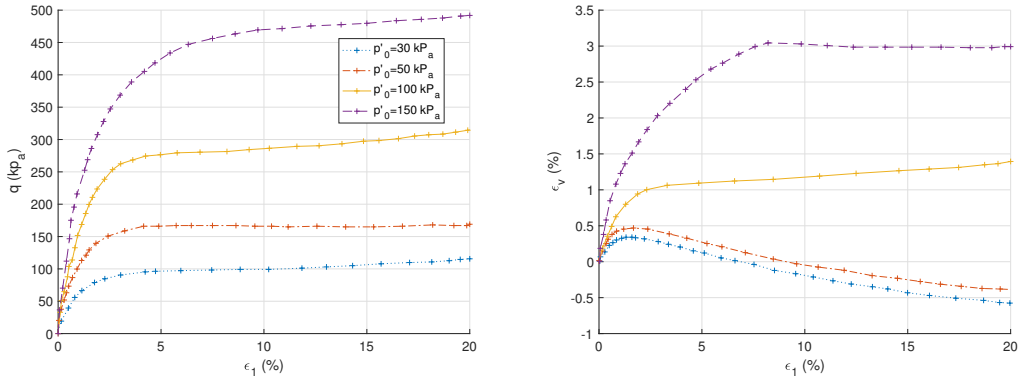

Figure 10. Response of the material under saturated drained triaxial tests - according to Hoang (2017).
Alt Text: $(q - \varepsilon_1)$ curves and $(\varepsilon_v - \varepsilon_1)$ curves showing the responses of the Gavet silt on drained triaxial test at 30 kP_a, 50 kP_a, 100 kP_a and 150 kP_a

of four drained triaxial tests was carried out. The initial confining pressures were as follows: 30 kP_a, 50 kP_a, 100 kP_a and 150 kP_a. Responses in the planes $(q,\ \varepsilon_1)$ and $(\varepsilon_v,\ \varepsilon_1)$ are presented in figure 10. Although all four samples were expected to be in the overconsolidation range, the response of the samples under initial consolidation pressures of 100 kP_a and 150 kP_a indicated a contractive response.

5.2. Description of the unsaturated triaxial tests

After the compaction procedure, the samples at the CBR mold dimensions were packed in a plastic film and stored in a standard room in our laboratory for at least 10 days in order to be sure that the suction became stable. This delay was empirically observed in the study by Hoang (2017). The samples were then shaped with a cutting device, as indicated in figure 11. The initial dimensions and characteristics of the samples are summarized in table 1. The samples were then placed in a standard triaxial cell. We

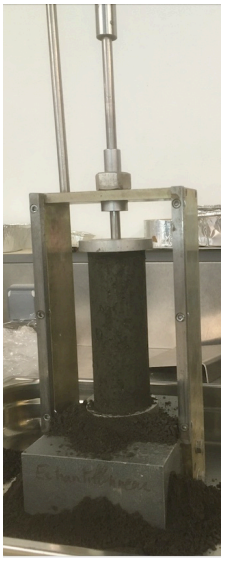

Figure 11. Cutting device for the soil samples.
Alt Text: Photograph of the cutting device of the soil samples.

ϕ (mm)	h (mm)	w (%)	ρ_s (g/cm^3)
54.0	112	10.5	2.72
ρ_d (g/cm^3)	e	S_r (%)	s (kP_a)
1.82	0.494	57.7	55.0

Table 1. Main dimensions and characteristics of the soil samples.

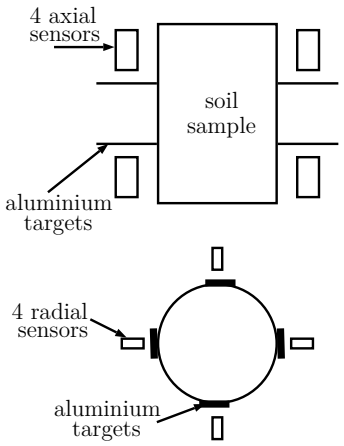

Figure 12. Sketch of the measurement device
Alt Text: Sketch showing the position of each contactless sensors.

used local inductive sensors to measure the deformations. In fact, the volume change cannot be measured with the pore water content changes. A sketch of the measurement device is presented in figure 12, and a photograph is presented in figure 13.

5.3. Results of the unsaturated triaxial tests

A series of three drained triaxial compressions were performed for three distinct confining pressures (in total stress): a simple compression at $p_0 = 0$, followed by two confined compressions at $p_0 = 100\ kP_a$ and $p_0 = 150\ kP_a$. Pictures of the state of the samples after being dismantled are presented shown in figure 14. We can clearly see the effect of the confining pressure on the failure mode. For the simple compression, a sub-vertical band is observed with an inclination of approximately 70°. The inclination of the shear band is approximately 60° for the test at 100 kP_a, while no macroscopic shear band is visible for the test at 150 kP_a The responses of this soil in terms of deviatoric stress and volume strain are presented in figure 15. During these tests, the initial suction before the isotropic compression was approximately 55 kP_a. The isotropic compression and the deviatoric compression were then performed in drained conditions without control or measurement of the suction. It was observed that the mass water content remained constant during the tests. Indeed, measurements of the mass water content on the samples dismantled at the end of the tests revealed no water loss.

5.4. Interpretation of the results

First, we should indicate that we were unable to assess the value of the capillary pressure ($p^{cap} = tr\left(\boldsymbol{\sigma}^{cap}\right)/3$ at the end of the isotropic compression in an objective manner with our standard experimental device. Consequently, we focus our work on the assessment of the capillary tensor at the failure state. To do so, it is convenient to indicate the failure points obtained in saturated and unsaturated conditions in the $(q - p)$ plane (see figure 16). It should be noted that in the present work, we adopt the standard definition of failure given by the elastoplasticity theory, i.e. the maximum stress that the elastoplastic solid can sustain and not the residual stress after the peak, for the following reasons. After the peak, the mathematical solution to the problem posed in

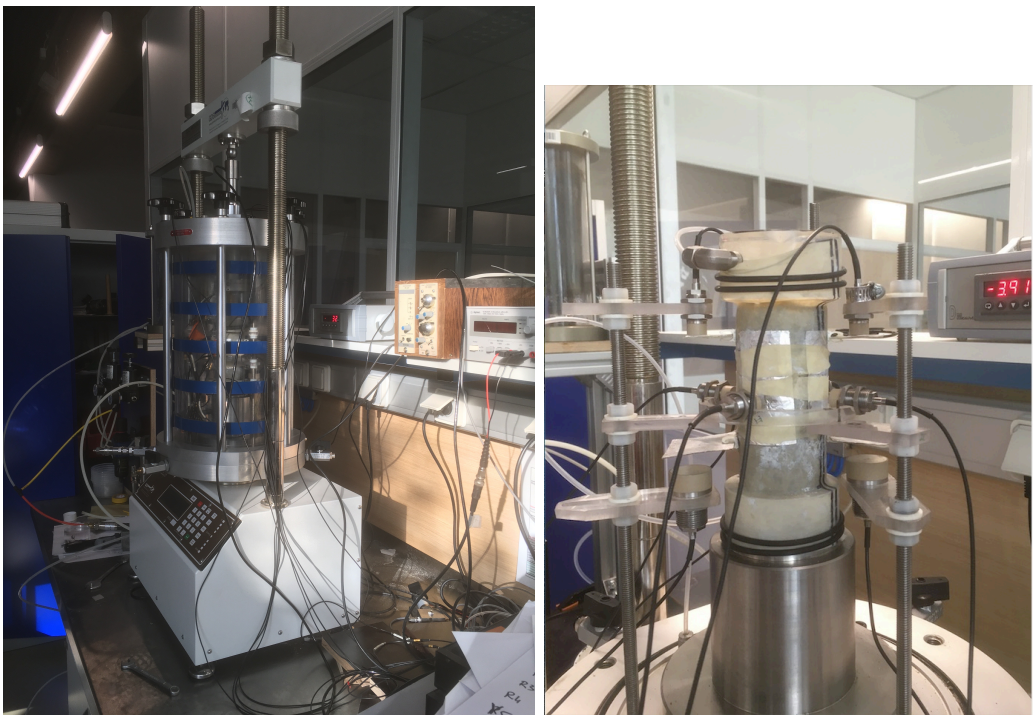

Figure 13. Picture of the experimental device.
Alt Text: 2 photographs of the triaxial device. On the left with the cell. On the right the cell is removed to show every sensors on the sample.

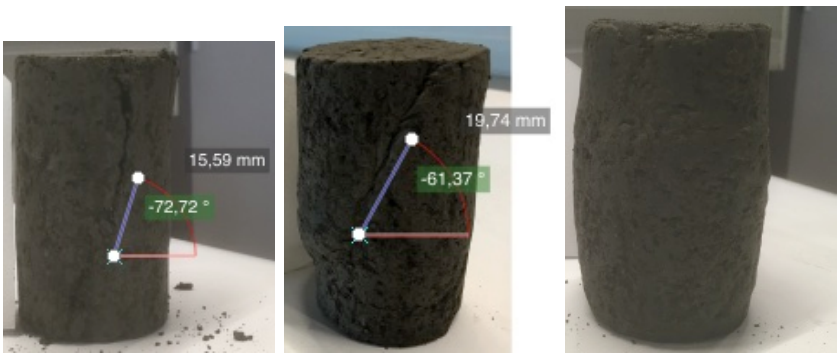

Figure 14. Pictures of the silt samples after the unsaturated drained triaxial tests: (a) simple compression, shear band angle $\approx 70°$, (b) test at 100 kP_a, shear band angle $\approx 60°$, (c) test at 150 kP_a, no visible macroscopic shear band.
Alt Text: 3 photographs of the 3 samples dismantled at the end of the 3 triaxial trials. The first two samples show a shear band while the third one no.

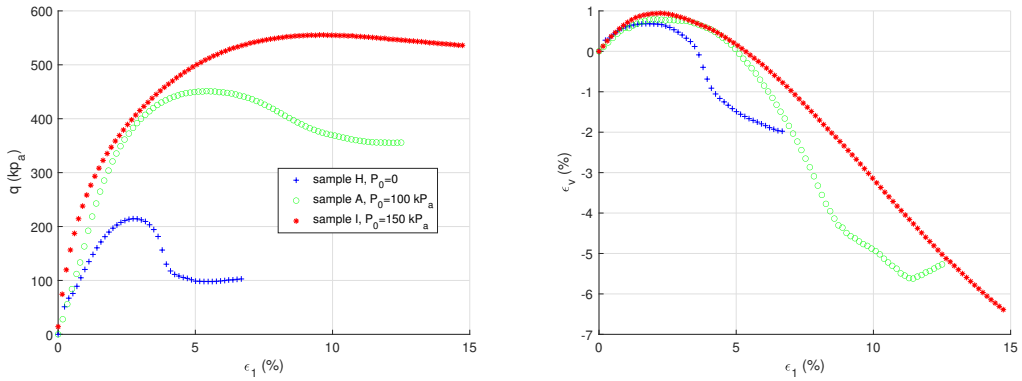

Figure 15. Response of the material under unsaturated drained triaxial tests. The initial suction before the isotropic compression was approximately 55 kP_a. The isotropic compression and the deviatoric compression were then performed in drained conditions without control or measurement of the suction.
Alt Text: $(q - \varepsilon_1)$ and $(\varepsilon_v - \varepsilon_1)$ curves showing the response of the Gavet silt to the unsaturated drained triaxial tests at 0, 100 kP_a and 150 kP_a

$p_0 = 0\ kP_a$	$p_0 = 100\ kP_a$	$p_0 = 150\ kP_a$
$p_f^{cap} = -64\ kP_a$	$p_f^{cap} = -40\ kP_a$	$p_f^{cap} = -26\ kP_a$

Table 2. Results in terms of capillary pressure at failure, using the assumption of a spherical capillary tensor. The initial suction is $s_0 \approx 55\ kP_a$, for the three tests.

the elastoplasticity framework is no longer unique. From a physical point of view, this translates into a post-peak response that is highly sensitive to the slightest defects in the sample or boundary conditions. Hence, we consider an analysis by working on samples deemed to be homogeneous. This approach aims to ensure the consistency of our study and minimize variables that could influence our conclusions.

In this figure, we did not link the failure points relating to unsaturated tests, since these failure points are not comparable from a constitutive point of view. In fact, their respective capillary tensors cannot be measured or controlled. Consequently, it is not possible to derive a cohesion and a friction angle expressed in total stress from these points. To estimate the capillary tensor that holds at failure for each of the three tests, we used the hypotheses presented in section 4.

The most simple approach is to assume a spherical capillary tensor that can be used as a conservative upper bound for the capillary stress that holds at failure. In such a case, $q = q'$, and the effective image point is the horizontal projected point on the Mohr-Coulomb envelope. In the present case, the capillary pressures obtained are presented in table 2. Next, the lower bound of the capillary stress that holds at failure was assessed with the equations (24) and (27), while the upper bound is presented with the questionable assumption of a drained triaxial path for the effective stress path, as presented in section 4. figure 17 presents the range of the possible image points that can be used on the effective Mohr-Coulomb envelope to assess the effective stress at failure, and therefore the capillary stress at failure. figure 18 presents the range of the acceptable capillary stress at failure. The following observations arise from these results:

(1) The assumption of a drained triaxial path for the effective stress as a response of the unsaturated sample has to be verified in further DEM simulations for a wider

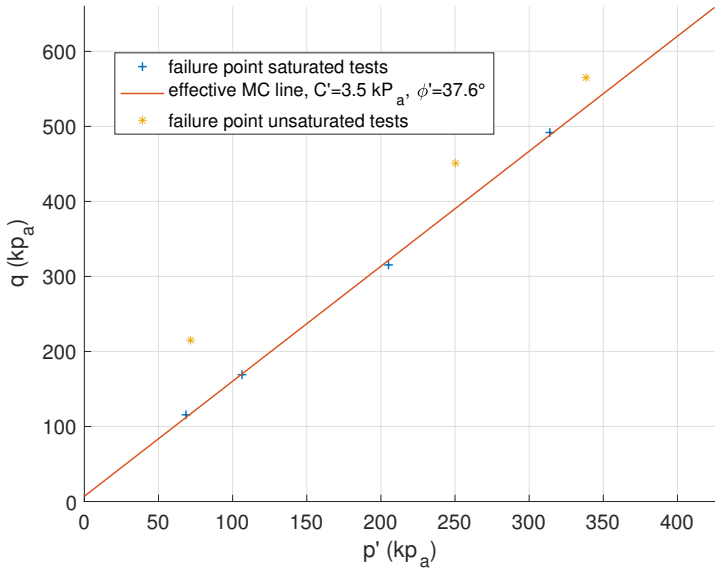

Figure 16. Failure points obtained for the saturated drained triaxial tests ($p_0' = 30,\ 50,\ 100,\ and\ 150\ kP_a$) and for the unsaturated drained triaxial tests ($p_0 = 0,\ 100,\ and\ 150\ kP_a$).
Alt text: $(q - p)$ plane showing the effective Mohr-Coulomb line and the failure points measured in total stress.

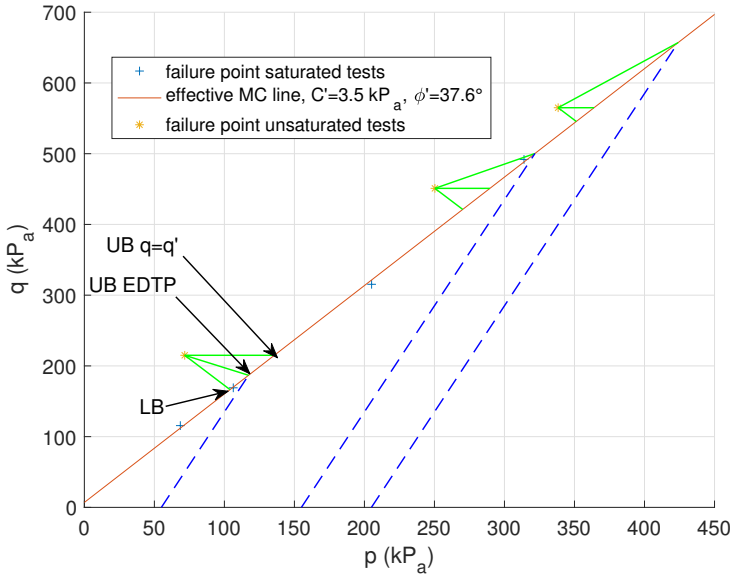

Figure 17. Range of effective stresses at failure to assess the capillary stress at failure. [LB]=lower bound, [UB q=q']=upper bound assuming a spherical capillary stress, [UB EDTP]=upper bound assuming an effective drained triaxial path. The dashed lines depict the effective stress path assumed using the upper limit for the initial capillary pressure $p_0^{capmax} = -s_0 \approx -55\ kP_a$.
Alt Text: $(q - p)$ plane showing the effective Mohr-Coulomb line and the the failure points measured in total stress as well as green lines that shows the assumed projection procedure to compute the capillary stress components.

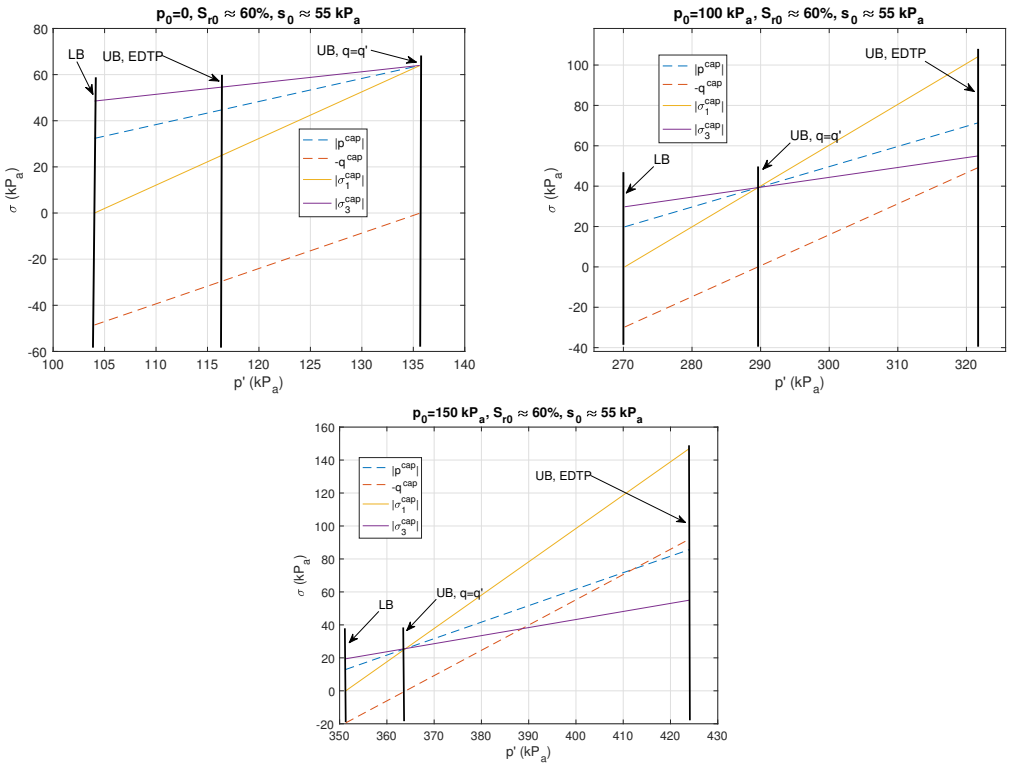

Figure 18. Range of capillary stresses at failure. [LB]=lower bound, [UB q=q']=upper bound assuming a spherical capillary stress, [UB EDTP]=upper bound assuming an effective drained triaxial path.
Alt Text: 3 graphs showing the possible range of the capillary stress components bounded by the assumptions developed in the present work. The 3 graphs show the results for the 3 trials done at 0, 100 kP_a and 150 kP_a.

$q'_{0LB}/q_0^{'sat}$	$q'_{100LB}/q_{100}^{'sat}$	$q'_{150LB}/q_{150}^{'sat}$
10.64	1.28	1.13
$q'_{0UB}/q_0^{'sat}$	$q'_{100UB}/q_{100}^{'sat}$	$q'_{150UB}/q_{150}^{'sat}$
15.04	1.38	1.17

Table 3. Effective shear strength gain obtained comparing the unsaturated case with the saturated case. [LB]=lower bound. [UB]=upper bound assuming a spherical capillary stress.

range of saturation regime and, if possible, in future experimental tests where proper image analysis is developed for the fluid phases.

(2) At present, in view of engineering practice, the proposed lower bound and the upper bound given by $q = q'$ seem reasonable enough and are very easy to assess, even with the use of standard triaxial devices. It should be stressed that the non-spherical lower bound must be considered to ensure that conservative computations are performed.

(3) In the context of our experimental results, we can quantify the gain in shear strength by considering the effective strength using the non-spherical lower bound or by avoiding unsaturated effects, as is frequently done in practice. To do so, we denote $\left[q_0^{'sat}, q_{100}^{'sat}, q_{150}^{'sat}\right]$ as the shear strength when performing saturated drained triaxial tests for an initial isotropic pressure $p'_0 = 0,\ 100\ kP_a,\ and\ 150\ kP_a$ and $[q'_{0LB}, q'_{100LB}, q'_{150LB}]$ the effective shear strength, assessed with the lower bound assumption, when performing unsaturated drained triaxial tests for an initial isotropic pressure $p_0 = 0,\ 100\ kP_a,\ and\ 150\ kP_a$. In the same way, we denote $[q'_{0UB}, q'_{100UB}, q'_{150UB}]$ when the effective shear strength is assessed with the spherical capillary stress assumption ($q = q'$). The table 3, yields the ratio $q'_{LB}/q^{'sat}$ and $q'_{UB}/q^{'sat}$. It is clear that the gain can be very significant at low confining pressures and less significant at upper confining pressures. Nevertheless, it could help to justify some practical analyses in the short term. We emphasize that considering a computation with the effective soil parameters and introducing a non-spherical capillary stress can lead to different conclusions than adding the apparent cohesion in the soil parameters.

6. Concluding remarks

In conclusion, the main results of this work are summarized below.

(1) The main difficulty in establishing a constitutive model with an effective stress formalism in the unsaturated domain relates to the fact that an unsaturated medium can be in static equilibrium for geometric configurations that are not acceptable in the saturated domain. This led us to propose a diagram illustrating the notions of effective strain (conjugated with its effective stress via the existence of a potential strain energy for the solid skeleton) and capillary strain resulting from the liquid-gas interfaces and fluid-solid interfaces (Madeo et al. (2013)). However, it is easy to observe that, in general, the total strain measured at the boundary of the sample does not decompose in an additive way into effective and capillary strains. Moreover, access to an experimental measurement of these two strain tensors remains a challenge at the present time. Nevertheless, the study by Duriez et al. (2018) tends to confirm that the identification of the total deformation with

the effective deformation is possible for compressive small deformations and for failure states.

(2) Based on these conceptual results, we propose an experimental procedure to be tested in future studies to identify the capillary tensor. It consists of performing a first desaturation on an initially saturated soil sample to obtain a desired suction or degree of saturation and then applying a loading path under unsaturated conditions. On a second identical sample, exactly the same strain path measured on the first sample is imposed at the boundary of the second sample, but under saturated conditions. If this strain path can be imposed, the difference between the total stress path of the first sample and the effective stress path of the second sample provides the capillary stress response. Otherwise, this means that the total strain cannot be identified with the effective strain for the unsaturated loading path considered. To our knowledge, such a procedure has not been tested. In a second step, we propose certain basic assumptions to evaluate the capillary tensor at failure. The objective is to identify an effective image point on the failure envelope obtained in saturated conditions that is admissible from a constitutive point of view. The difference between the total stress measured at failure and the effective stress given by the image point then provides an assessment of the capillary effects. We first assume that all components of the capillary tensor are negative in the unsaturated regime. This provides a lower bound of the effective stress image point. This lower bound is reached for $q' < q$. An upper bound such that $q' > q$ is found to be infinite with the latter assumption. Therefore, we propose using the assumption of an isotropic capillary tensor to evaluate a conservative upper bound as a first approach. This is equivalent to considering $q = q'$.

(3) We carried out a campaign of unsaturated triaxial tests with a standard experimental device and analysed the results at failure, on the basis of the assumptions given above. For the considered silt under an initial suction level of 55 kP_a, it was observed, inter alia, that the apparent total strength was 10 times the effective strength for the compression at $\sigma_3 = 0$, while this ratio decreased to 1.3 and 1.1 for compressions at $\sigma_3 = 100\ kP_a$ and $\sigma_3 = 150\ kP_a$.

7. Appendix 1

In the next subsections, we propose to develop the mathematical expressions of the capillary tensor $\boldsymbol{\sigma^{cap}}$ that holds at failure by adopting a Mohr-Coulomb failure criterion. $\boldsymbol{\sigma^{cap}}$ is derived from the difference of the total stress $\boldsymbol{\sigma}$ and of the effective stress $\boldsymbol{\sigma'}$, assuming that it is possible to experimentally determine two constitutively comparable states from the unsaturated case and the saturated case.

7.1. Spherical capillary stress case

Let us consider the Mohr diagram in figure 19. C' and φ' denote the cohesion and the friction angle measured considering the effective stress with saturated samples, while C and φ denote the cohesion and the friction angle virtually measured with unsaturated samples subjected to the same $\boldsymbol{\sigma^{cap}}$ for distinct lateral stresses σ_3.

If we assume a spherical capillary tensor, then $\boldsymbol{\sigma^{cap}}$ reduces to a single point in the Mohr diagram and the following relationships hold:

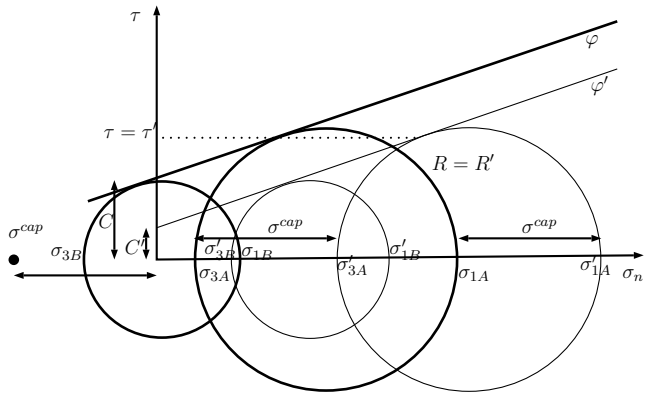

Figure 19. Mohr circles considering a spherical capillary tensor. Total stress circles are only translated of the quantity σ^{cap}. Strong lines are used for total stress and thin lines for effective stress.
Alt Text: Sketch of Mohr circles considering a spherical capillary tensor for computing the capillary pressure.

$$\tau = \tau' \tag{32}$$

and

$$\frac{\sigma_1 - \sigma_3}{2} = \frac{\sigma'_1 - \sigma'_3}{2} \tag{33}$$

consequently we have the following result :

$$\boxed{\sigma_{ij}^{cap} = \sigma^{cap}\delta_{ij} \Leftrightarrow R = R'} \tag{34}$$

with R is the radius of the Mohr circle in the unsaturated case and R' is the radius in the saturated case. In fact, it is trivial to prove that $R = R' \Rightarrow \sigma_1^{cap} = \sigma_3^{cap}$. In other words, the change of the radius of two comparable stress states from a constitutive point of view provides a measure of the deviator part of the capillary tensor.

Furthermore,

$$\frac{\sigma_1 - \sigma_3}{2} = \frac{\tau}{\cos\varphi} = \frac{\tau'}{\cos\varphi'} \Rightarrow \varphi = \varphi' \tag{35}$$

Thus, in the spherical case, we get only a pure horizontal translation of the failure envelope. For soils, the translation of the Mohr-Coulomb line is given by the relationship

$$\tan\varphi' = -\frac{C - C'}{\sigma^{cap}} \tag{36}$$

and we get the classical final result:

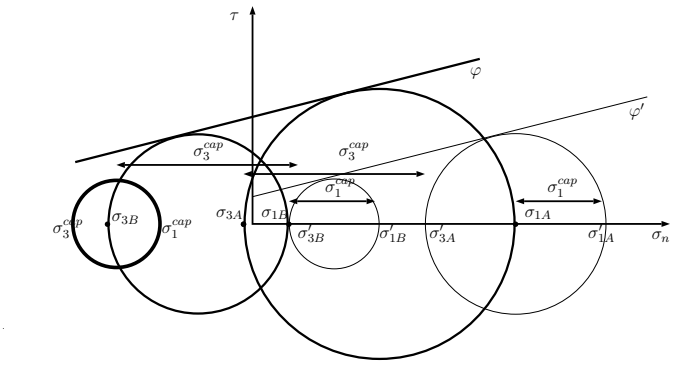

Figure 20. Mohr circles considering a non-spherical capillary tensor under axisymmetric conditions.
Alt Text: Sketch of Mohr circles considering a non spherical capillary tensor under axisymmetric conditions for computing the components of the capillary stress tensor.

$$\boxed{\sigma^{cap} = -\frac{C - C'}{\tan\varphi'}} \tag{37}$$

which provides the apparent cohesion of unsaturated soils.

7.2. Non-spherical capillary tensor under axisymmetric conditions

In this case $R \neq R'$. The Mohr diagram to be considered is given in figure 20. Because the capillary tensor is no longer spherical, we have $\tau \neq \tau'$.

In the first step, we prove that $\varphi = \varphi'$ remains true. From a qualitative point of view, $R \neq R'$ implies a shift plus a dilation of the failure envelop. This geometrical transformation keeps $\varphi = \varphi'$ for the Mohr-Coulomb envelop. The Mohr-Coulomb relationship can also be written in terms of $t = 1/2\,(\sigma_1 - \sigma_3)$ and $s = 1/2\,(\sigma_1 + \sigma_3)$, as follows:

$$t = s\sin\varphi + C\cos\varphi \tag{38}$$

Consequently, we get :

$$t'_A + \frac{\sigma_1^{cap} - \sigma_3^{cap}}{2} = \left(s'_A + \frac{\sigma_1^{cap} + \sigma_3^{cap}}{2}\right)\sin\varphi + C\cos\varphi \tag{39}$$

and

$$t'_B + \frac{\sigma_1^{cap} - \sigma_3^{cap}}{2} = \left(s'_B + \frac{\sigma_1^{cap} + \sigma_3^{cap}}{2}\right)\sin\varphi + C\cos\varphi \tag{40}$$

Making the difference between equations (39) and (40), we get:

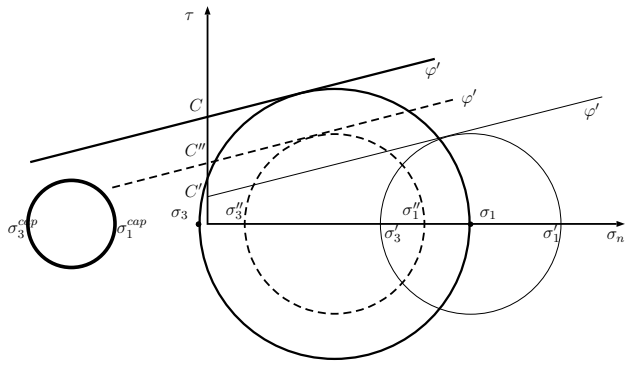

Figure 21. Mohr circles considering a non-spherical capillary tensor under axisymmetric conditions and the intermediate stress state $\boldsymbol{\sigma''}$ considered.
Alt Text: Sketch of Mohr circles considering a non spherical capillary tensor under axisymmetric conditions for computing the components of the capillary stress tensor highlighting the intermediate state.

$$t'_A - t'_B = (s'_A - s'_B)\sin\varphi \tag{41}$$
$$\Leftrightarrow (s'_A - s'_B)\sin\varphi' = (s'_A - s'_B)\sin\varphi \tag{42}$$
$$\Leftrightarrow \varphi = \varphi' \tag{43}$$

To asses the components of the capillary tensor, we introduce the fictive stress state $\boldsymbol{\sigma''}$, who's the Mohr circle is concentric to the one in the unsaturated configuration but keeps the radius of the Mohr circle in the saturated configuration. A sketch of this fictive stress is displayed in figure 21.

Thus, we get

$$\frac{\sigma_1^{cap} + \sigma_3^{cap}}{2} = -\frac{C'' - C'}{\tan\varphi'} \tag{44}$$

and, in virtue of the Mohr-Coulomb relationship, we also have :

$$t' + \frac{\sigma_1^{cap} - \sigma_3^{cap}}{2} = \left(s' + \frac{\sigma_1^{cap} + \sigma_3^{cap}}{2}\right)\sin\varphi' + C\cos\varphi' \tag{45}$$
$$\Leftrightarrow t' + \frac{\sigma_1^{cap} - \sigma_3^{cap}}{2} = s'\sin\varphi' - (C'' - C')\cos\varphi' + C\cos\varphi' \tag{46}$$
$$\Leftrightarrow \frac{\sigma_1^{cap} - \sigma_3^{cap}}{2} = (C - C'')\cos\varphi' \tag{47}$$

thus

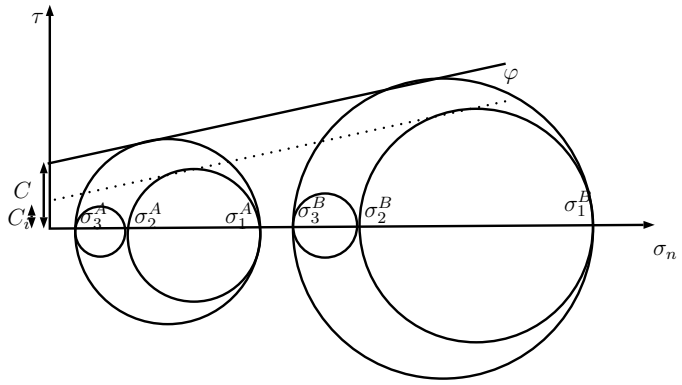

Figure 22. Envelop of the Mohr circle using the major and the intermediate stress under a constant Lode's angle triaxial path.
Alt Text: Sketch of Mohr circles considering a non spherical capillary tensor under $3d$ conditions for computing the components of the capillary stress tensor.

$$\boxed{\begin{cases} \frac{\sigma_1^{cap}+\sigma_3^{cap}}{2} = -\frac{C''-C'}{\tan\varphi'} \\ \frac{\sigma_1^{cap}-\sigma_3^{cap}}{2} = (C-C'')\cos\varphi' \end{cases}} \tag{48}$$

To conclude this section, equation (48) provides a good estimator of the components of the capillary stress tensor that hold at failure, if two failure points under unsaturated conditions are observed to be aligned parallel to the effective Mohr-Coulomb line.

7.3. Non-spherical capillary stress tensor under general 3D conditions

For the general 3D case, we have to consider a particular true triaxial loading path to be able to give an interpretation to the intermediate stress. Let us consider a true drained triaxial loading path under constant Lode's angle. Under such a stress path, we get the following relationship (see figure 22):

$$\frac{\sigma_1^A - \sigma_2^A}{\sigma_1^A - \sigma_3^A} = \frac{\sigma_1^B - \sigma_2^B}{\sigma_1^B - \sigma_3^B} \tag{49}$$

The proof that equation (49) $\Leftrightarrow$ $\theta^A = \theta^B$ is provided in the appendix 8, where θ^A and θ^B are the respective Lode's angles of the stresses A and B.
Consequently, the Mohr circles made of σ_1 and σ_2 follows a similar envelop as the failure envelop with an expansion factor. For the case of the Mohr-Coulomb envelop, it means that the friction angle is maintained. We can introduced an intermediate cohesion denoted C_i, which has no physical meanings but can mathematically describe the envelop of the intermediate stress (see figure 22).
Using such loading paths, the results obtained in axisymmetrical conditions can be extended in a similar manner and lead to the expressions given in equation (50).

$$\boxed{\begin{cases} \frac{\sigma_1^{cap}+\sigma_3^{cap}}{2} = -\frac{C''-C'}{\tan\varphi'} \\ \frac{\sigma_1^{cap}-\sigma_3^{cap}}{2} = (C-C'')\cos\varphi' \\ \frac{\sigma_1^{cap}-\sigma_2^{cap}}{2} = (C_i-C_i'')\cos\varphi' \end{cases}} \tag{50}$$

In practice, the formulae in equation (37), equation (48) and equation (50) may be of interest in cases where the experimental conditions allow for the observation of $\varphi = \varphi'$ and it has been ensured that σ_0^{cap} at the beginning of the triaxial compression is the same for the three tests. Therefore, it seems that σ_f^{cap} at failure is likely to be the same for all three tests. Thus, these formulas can be used in a standard way to perform a linear regression and to minimize experimental errors.

8. Appendix 2

Proof of :

$$\frac{\sigma_1^A - \sigma_2^A}{\sigma_1^A - \sigma_3^A} = \frac{\sigma_1^B - \sigma_2^B}{\sigma_1^B - \sigma_3^B} \Leftrightarrow \ \theta^A = \theta^B \tag{51}$$

with θ^A and θ^B the respective Lode's angles of the stresses A and B.
Let us denote :

$$I_1 = \mathrm{tr}\left(\boldsymbol{\sigma}\right);\ \boldsymbol{s} = \boldsymbol{\sigma} - \frac{I_1}{3}\boldsymbol{I};\ J_2 = \mathrm{tr}\left(\boldsymbol{s}^2\right);\ J_3 = \mathrm{tr}\left(\boldsymbol{s}^3\right) \tag{52}$$

with such notations we have:

$$\cos\left(3\theta\right) = \frac{\sqrt{6}J_3}{\sqrt{J_2^3}} = \frac{\sqrt{6}\left(s_1^3+s_2^3+s_3^3\right)}{\sqrt{\left(s_1^2+s_2^2+s_3^2\right)^3}} \tag{53}$$

for the sake of clarity, we will also denote

$$Q = \frac{\sigma_1^B - \sigma_2^B}{\sigma_1^B - \sigma_3^B} \tag{54}$$

consequently we have:

$$\sigma_2^A = \sigma_1^A - Q\left(\sigma_1^A - \sigma_3^A\right) \tag{55}$$

and after some few algebra we get :

$$\begin{cases} s_1^A = \frac{1+Q}{3}\left(\sigma_1^A - \sigma_3^A\right) \\ s_2^A = \frac{1-2Q}{3}\left(\sigma_1^A - \sigma_3^A\right) \\ s_3^A = \frac{Q-2}{3}\left(\sigma_1^A - \sigma_3^A\right) \end{cases} \tag{56}$$

676 denoting $C = \left(\sigma_1^A - \sigma_3^A\right)/3$ we get:

$$\cos\left(3\theta^A\right) = \frac{\sqrt{6}C^3\left[(1+Q)^3 + (1-2Q)^3 + (Q-2)^3\right]}{C^3\sqrt{\left[(1+Q)^2 + (1-2Q)^2 + (Q-2)^2\right]^3}} \tag{57}$$

677 then it is also easy to show that:

$$\begin{cases} 1+Q = \frac{s1^B}{\left(\sigma_1^B - \sigma_3^B\right)} \\ 1-2Q = \frac{s2^B}{\left(\sigma_1^B - \sigma_3^B\right)} \\ Q-2 = \frac{s3^B}{\left(\sigma_1^B - \sigma_3^B\right)} \end{cases} \tag{58}$$

678 and replacing these expressions into equation (57), we finally get

$$\cos\left(3\theta^A\right) = \frac{\sqrt{6}\left((s_1^B)^3 + (s_2^B)^3 + (s_3^B)^3\right)}{\sqrt{\left((s_1^B)^2 + (s_2^B)^2 + (s_3^B)^2\right)^3}} = \cos\left(3\theta^B\right) \tag{59}$$

679 9. Data Availability

680 The authors confirm that the data supporting the findings of this study are available
681 within the article.

682 References

683 Alonso, E., Pereira, J.-M., Vaunat, J., & Olivella, S. (2010). A microstructurally based effective
684 stress for unsaturated soils. *Géotechnique*, *60*, 913-925(12).
685 Alonso, E.E., Gens, A., & Josa, A. (1990). A constitutive model for partially saturated soils.
686 *Geotechnique*, *40(3)*, 405-430.
687 Arairo, W., Prunier, F., Djéran-Maigre, I., & Darve, F. (2012). A new insight into modelling
688 the behaviour of unsaturated soils. *Internationnal Journal for Numerical and Analytical*
689 *Methods in Geomechanics*, *37*, 2629-2654. (DOI: 10.1002/nag.2151)
690 Biot, M. A. (1955). Theory of elasticity and consolidation for a porous anisotropic solid.
691 *Journal of Applied Physics*, *26*(2), 182-185.
692 Bishop, A.M., & Blight, G.E. (1963). Some aspects of the effective stress in saturated and
693 unsaturated soils. *Géotechnique*, *13(3)*, 177-197.
694 Bruno, A.W.., Gallipoli, D., & Mendes, J. (2021). Hydromechanical behaviour of two unsat-
695 urated silts: laboratory data and model predictions. *Canadian Geotechnical Journal*, *59*,
696 837-846.

Chateau, X., & Dormieux, L. (1995). Homogenization of a non-saturated porous medium: Hill's lemma and applications. *C. R. Acad. Sci. Paris, Série II*, *320*, 627–634.

Christoffersen, J., & Hutchinson, J. (1979). A class of phenomenological corner theories of plasticity. *Journal of the Mechanics and Physics of Solids*, *27*(5), 465-487.

Colman, B.D., & Gurtin, M. (1967). Thermodynamics with internal state variables. *Journal of Chemistry and Physics*, *47*, 597-613.

Coussy, O. (2004). *Poromechanics*. Wiley.

Coussy, O., & Dangla, P. (2002). Approche énergétique du comportement des sols non saturés. In O. Coussy & J.M. Fleureau (Eds.), *Mécanique des sols non saturés* (p. 137-174). traité MIM Hermes Lavoisier.

Cowin, S. C., & Nunziato, J. W. (1983). Linear elastic materials with voids. *Journal of Elasticity*, *13*(2), 125–147.

Darve, F., Arulanandan, K., & Scott, R. F. (1993). Liquefaction phenomenon: Modelling, stability and uniqueness, international conference, verification of numerical procedures for the analysis of soil liquefaction problems. In *Verification of numerical procedures for the analysis of soil liquefaction problems, international conference, verification of numerical procedures for the analysis of soil liquefaction problems* (p. 1305-1320). California: Balkema A;. Retrieved from `https://www.tib.eu/de/suchen/id/BLCP`

De Buhan, P., & Dormieux, L. (1996). On the validity of the effective stress concept for assessing the strength of saturated porous materials: A homogenization approach. *Journal of the Mechanics and Physics of Solids*, *44*(10), 1649-1667.

Desai, C., & Siriwardane, H. (1984). *Constitutive laws for engineering materials, with emphasis on geologic materials*. Prentice-Hall.

DiMaggio, F.L., & Sandler, I.S. (1971). Material model for granular soils. *Journal of the Engineering Mechanics Division*, *97*(3), 935-950.

Duriez, J., Eghbalian, M., Wan, R., & Darve, F. (2017). The micromechanical nature of stresses in triphasic granular media with interfaces. *Journal of the Mechanics and Physics of Solids*, *99*, 495–511.

Duriez, J., & Wan, R. (2016). Stress in wet granular media with interfaces via homogenization and discrete element approaches. *Journal of Engineering Mechanics*, *142(12)*.

Duriez, J., & Wan, R. (2017a). Contact angle mechanical influence for wet granular soils. *Acta Geotechnica*, *12*(1), 67–83.

Duriez, J., & Wan, R. (2017b). Subtleties in discrete-element modelling of wet granular soils. *Géotechnique*, *67*(4), 365–370.

Duriez, J., & Wan, R. (2018). A micromechanical μUNSAT effective stress expression for stress-strain behaviour of wet granular materials. *Geomechanics for Energy and the Environment*, *15*, 10–18.

Duriez, J., Wan, R., Pouragha, M., & Darve, F. (2018). Revisiting the existence of an effective stress for wet granular soils with micromechanics. *Internationnal Journal for Numerical and Analytical Methods in Geomechanics*, *42*(8), 959–978.

Eshelby, J.D. (1957). The determination of the elastic field of an ellipsoidal inclusion, and related problems. In *Proceedings of the royal society a: Mathematical, physical and engineering sciences* (Vol. 241(1226), p. 376-396).

Farahnak, M., Wan, R., Pouragha, M., Eghbalian, M., Nicot, F., & Darve, F. (2021). Micromechanical description of adsorptive-capillary stress in wet fine-grained media. *Computers and Geotechnics*, *137*, 104047. Retrieved from `https://www.sciencedirect.com/science/article/pii/S0266352X21000501`

Froiio, F., & Roux, J.-N. (2011). Numerical stress probing on a 2d model granular material. *Particle-Based Methods II - Fundamentals and Applications*, 72-83.

Gray, W.G., & Schrefler, B.A. (2007). Analysis of the solid phase stress tensor in multiphase porous media. *International Journal for Numerical and Analytical Methods in Geomechanics*, *31*, 541-581.

Gurtin, M. E., & Murdoch, A. I. (1975). A continuum theory of elastic material surfaces. *Archive for Rational Mechanics and Analysis*, *57*(4), 291-323.

Hoang, N.L. (2017). *Etude des propriétés hydromécaniques d'un sable limoneux* (Unpublished doctoral dissertation). ENTPE, Université de Lyon.

Khalili, N., & Khabbaz, M.H. (1998). A unique relationship for χ for the determination of the shear strengh of unsaturated soils. *Géotechnique*, *48(5)*, 681-687.

Lade, P. V., & De Boer, R. (1997). The concept of effective stress for soil, concrete and rock. *Géotechnique*, *47*(1), 61-78.

Lanier, J., & Bloch, J. (1989). Essais à volume constant réalisés sur une presse tridimensionnelle. In J. Reynouard (Ed.), *Greco geomaterials* (p. 240-43). INSA Lyon.

Lu, N., & Likos, W. (2006). Suction stress characteristic curve for unsaturated soil. *Journal of Geotechnical and Geoenvironmental Engineering*, *132*(2), 131-142.

Madeo, A., dell'Isola, F., & Darve, F. (2013). A continuum model for deformable, second gradient porous media partially saturated with compressible fluids. *Journal of the Mechanics and Physics of Solids*, *61*(11), 2196 - 2211.

Mori, T., & Tanaka, K. (1973). Average stress in matrix and average elastic energy of materials with misfitting inclusions. *Acta Metallurgica*, *21*(5), 571-574.

Nikooee, E., Habibagahi, G., Hassanizadeh, S., & Ghahramani, A. (2013). Effective stress in unsaturated soils: A thermodynamic approach based on the interfacial energy and hydromechanical coupling. *Transp Porous Med*, *96*, 369-396. (DOI: 10.1007/s11242-012-0093-y)

Oller, S. (2014). Homogenization theory. In L. N. on Numerical Methods in Engineering & Sciences (Eds.), *Numerical simulation of mechanical behavior of composite materials.* Springer, Cham.

Rojas, E., & Chávez, O. (2013). Volumetric behavior of unsaturated soils. *Canadian Geotechnical Journal*, *50*, 209-222.

Roux, J.-N., & Combe, G. (2002). Quasistatic rheology and the origins of strain. *Comptes Rendus Physique*, *3*.

Rumpf, H. (1962). The strength of granules and agglomerates. *Agglomeration*, 379–418.

Scholtes, L., Hicher, P.Y., Nicot, F., Chareyre, B., & Darve, F. (2009). On the capillary stress tensor in wet granular materials. *International Journal for Numerical and Analytical Methods Geomechanics*, *33*, 1289-1313.

Schwan, B. (2023). Microstructural interpretation of effective stress equations for unsaturated sands. *International Journal of Geo-Engineering*, *14:4*. (DOI: https://doi.org/10.1186/s40703-022-00181-8)

Sibille, L., Hadda, N., Nicot, F., Tordesillas, A., & Darve, F. (2015). Granular plasticity, a contribution from discrete mechanics. *Journal of the Mechanics and Physics of Solids*, *75*, 119-139.

Skempton, A. W. (1954). The pore-pressure coefficients A and B. *Géotechnique*, *4*(4), 143-147.

Skempton, A. W., & Bjerrum, L. (1957). A contribution to the settlement analysis of foundations on clay. *Géotechnique*, *7*(4), 168-178.

Terzaghi, K. (1936). The shearing resistance of saturated soils and the angle between the planes of shear. In 1^{st} *international conference for soil mechanics and foundation engineering* (Vol. 1, pp. 54–56). Cambridge.

Weber, R., Romero, E., & Lloret, A. (2022). Shear strength and yield surface of a partially saturated sandy silt under generalized stress states. *Canadian Geotechnical Journal*, *59*, 1188-1204.

Zhou, T., Ioannidou, K., Masoero, E., Mirzadeh, M., Pellenq, R. J.-M., & Bazant, M. Z. (2019). Capillary stress and structural relaxation in moist granular materials. *Langmuir*, *35*(12), 4397-4402. Retrieved from `https://doi.org/10.1021/acs.langmuir.8b03400` (PMID: 30798608)